Quantum calibrated magnetic force microscopy

Baha Sakar [1,2,*] Yan Liu [3,4,*,†] Sibylle Sievers,[1] Volker Neu,[5] Johannes Lang [4] Christian Osterkamp [4]
Matthew L. Markham [6] Osman Öztürk,[2] Fedor Jelezko,[4] and Hans W. Schumacher[1]

[1]*Physikalisch-Technische Bundesanstalt, 38116 Braunschweig, Germany*
[2]*Gebze Technical University, Department of Physics, 41400, Kocaeli, Turkey*
[3]*Beijing Academy of Quantum Information Sciences, Beijing 100193, China*
[4]*Institute for Quantum Optics, Ulm University, 89081 Ulm, Germany*
[5]*Leibniz IFW Dresden, 01069 Dresden, Germany*
[6]*Element Six Global Innovation Centre, Oxfordshire, OX11 0QR, United Kingdom*

We report the quantum calibration of a magnetic force microscope (MFM) by measuring the two-dimensional magnetic stray-field distribution of the MFM tip using a single nitrogen vacancy (NV) center in diamond. From the measured stray-field distribution and the mechanical properties of the cantilever a calibration function is derived allowing to convert MFM images to quantum calibrated stray-field maps. This approach overcomes limitations of prior MFM calibration schemes and allows quantum calibrated nanoscale stray-field measurements in a field range inaccessible to scanning NV magnetometry. Quantum calibrated measurements of a stray-field reference sample allow its use as a transfer standard, opening the road towards fast and easily accessible quantum traceable calibrations of virtually any MFM.

Quantitative nanoscale stray-field measurements are a prerequisite for reliable and sound nanomagnetic research [1–3]. However, magnetic force microscopy (MFM), the most versatile tool for nanomagnetic imaging [4,5], generally provides qualitative stray-field information, only [6]. Common approaches to quantitative MFM (qMFM) [7–10] rely on simplifying assumptions on the magnetic tip [11–13] or the stray-field distribution of a calibration sample [9,14–19] which are hard to validate independently [10,11,20]. Few groups made attempts to directly characterize the magnetic stray-field distribution of MFM tips through the Hall effect [21,22] and by Lorentz tomography or holography [20,23,24]. Hall sensors, however, have a limited resolution due to the typical Hall cross dimensions of some 100 nm and Lorentz microscopy-based techniques require complex data postprocessing.

Scanning magnetometry with single diamond nitrogen vacancy (NV) centers opens a new path towards quantum-based quantitative nanoscale field measurements [2,25,26]. However, it is comparably slow and does not allow quantitative measurements in the relevant field range of many nanomagnetic materials of a few ten to a few hundred mT. Here, we report quantum calibration of MFM (QuMFM) by measuring the MFM tip's stray-field distribution using an NV center as a quantum sensor [27]. Using QuMFM we quantitatively measure the stray-field distribution of a typical MFM calibration sample with field amplitudes up to 100 mT, opening the road towards quantum traceable calibration of virtually any MFM.

NV measurements of the MFM tip's stray field are performed in a confocal microscope with bottom optical access and an integrated MFM on top [Fig. 1(a)]. The NV centers were prepared by 2.5-keV ^{15}N implantation into a thin layer of ultrapure isotopically enriched diamond (99.99% ^{12}C) that was epitaxially grown on the (001) surface of electronic-grade type IIa bulk diamond (Element Six, nitrogen concentration <6 ppb, often <1 ppb, typical NV concentration <0.3 ppb). For efficient photoluminescence detection the bulk diamond is shaped as a half-sphere structure, forming a solid immersion lens (SIL). Its upper planar surface is oriented along the *x-y* plane of the MFM. The selected single NV center with a photon rate of $1.2\,\mathrm{Mcs^{-1}}$ is situated 3.6 nm below the surface as derived from proton magnetic resonance [28] (see Supplemental Material [29]). The NV axis is oriented along [111] and has a nominal angle $\theta = (54.75 \pm 1)^\circ$ to the surface normal [Fig. 1(b)], with the uncertainty resulting from the miscut angle. The MFM tip was first scanned over the NV center in intermittent contact mode over a $2 \times 2\,\mu\mathrm{m}^2$ area to capture the surface topography. Then, the tip was scanned at a measurement height (i.e., the distance between the tip apex and the surface) of $z_{\mathrm{tot}} = 80$ nm above the surface with 100-nm step size and an optically detected magnetic resonance (ODMR) spectrum [30] was measured at each pixel. ODMR measures the shift of the Zeeman-split NV center spin-resonance frequencies $f_\pm$ induced by the tip stray field B^{tip} [Fig. 1(c)]. The NV spin states are optically accessed by the difference in fluorescence of $m_s = 0$ and $m_s = \pm 1$ states. Optical excitation polarizes the $m_s = 0$ state and a resonant microwave transfers the population to the "dark" ($m_s = \pm 1$) states with reduced fluorescence. We used π-pulse ODMR for the field sensing, to prepare near-100% spin population resulting in 30% contrast.
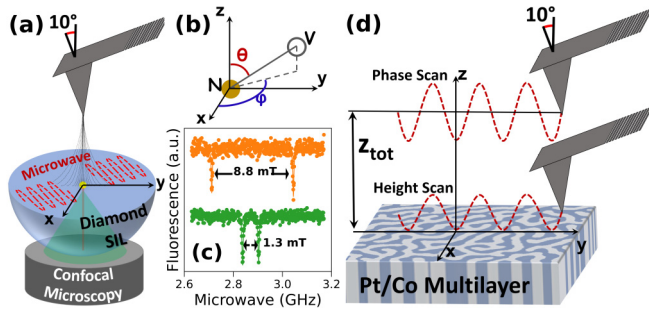
FIG. 1. Experimental setup. (a) NV-based stray-field measurements of an MFM tip. When scanning the MFM tip over the sample an ODMR spectrum is measured at every point. (b) Coordinate system of the measurements. The orientation of the NV axis is given by the polar angle θ and the azimuthal angle φ. (c) Typical ODMR spectrum for two different tip stray fields (fluorescence signal as function of microwave frequency). The curves are offset for clarity. The magnitude of the tip stray field at the position of the NV center and field angle β with respect to the NV center axis are derived from the splitting and offset of the resonance lines. (d) Principle of MFM measurements comprising a topography scan in intermittent contact mode and a phase scan at a tip-sample distance z_{tot} of 80 nm. The phase signal of the cantilever oscillation as a function of lateral tip position is collected as the MFM raw data.

The magnetic field sensitivity of the NV center of $0.54\ \frac{\mu T}{\sqrt{Hz}}$ is determined by the linewidth of its ODMR spectrum and by the photon collection efficiency. From the resonance frequencies the magnitude of the magnetic induction $B^{\text{tip}} = |\vec{B}^{\text{tip}}|$ and its angle $\beta = \sphericalangle(\overrightarrow{NV}, \vec{B}^{\text{tip}})$ [cf. Fig. 2(c)] with respect to the NV axis are derived (see Supplemental Material [29]). $B = \mu_0 H$ is given in units T with μ_0 the magnetic field constant and H the magnetic field in units Am^{-1}. Since in the literature B and H are often both referred to as "magnetic field," we will in the following use this term for simplicity.

The quantum calibrated low-moment MFM tip (MFM_LM, TipsNano) is coated by 20-nm CoCr with nominal tip radius of 30 nm. Scanning the metallic MFM tip near the NV center leads to a reduced fluorescence allowing to align the tip over the NV center with 200-nm uncertainty. In the intermittent contact mode, a free rms oscillation amplitude

of 10 nm was set with a setpoint of 3 nm during the surface scan. For the NV tip field measurements at $z_{\text{tot}} = 80$ nm the free-oscillation amplitude was reduced to 3 nm.

Figure 2 shows the stray-field distribution of the MFM tip measured at room temperature and zero applied field. B^{tip} [Fig. 2(a)] shows a rotation-symmetric maximum with the tip near the NV center sharply dropping towards the edges. In the 2D plot of the field angle β [Fig. 2(b)] the white dotted line marks the projection of the NV axis with azimuthal angle $\varphi = 119°$ [Fig. 1(b)]. β is mirror symmetric around φ as expected for a rotation-symmetric tip stray field. The variation of β along the axis is illustrated in Fig. 2(e). It sketches the stray-field lines of a pointlike tip in the plane defined by the surface normal and the NV axis. The red arrows indicate the NV axis, tilted by $\theta = 54.75°$ with respect to the surface normal, for three different relative positions of tip and NV center. At (1) the field and the NV axis are parallel. The corresponding region (1) on the top left of Fig. 2(b) is characterized by low angles (dark blue). At (2) the tip is positioned above the NV center with $\vec{B}^{\text{tip}}$ perpendicular to the surface and hence $\beta \approx \theta$. (3) reveals values around 90° with the field lines almost perpendicular to the NV axis [dark red in Fig. 2(b)]. The observed decay of β beyond (3), where B^{tip} is low is attributed to spurious background fields caused by field contributions from upper parts of the tip or magnetic components in the MFM system. Figure 2(c) shows a map of the field component parallel to the NV axis $B^{\text{tip}}_{||} = B^{\text{tip}}\cos\beta$. Again, the NV axis and the three configurations of Fig. 2(e) are marked. At (1), since $\cos\beta \approx 1$, $B^{\text{tip}}_{||}$ shows large values. Between (1) and (2) a maximum is found. Its position is determined by the competition between the decrease of $\cos\beta$ and the increase of B^{tip} with decreasing distance of tip and NV center. When following the dashed line to the lower right from (2) to (3) B^{tip} decreases strongly with distance leading to a decrease of $B^{\text{tip}}_{||}$.

In free space the knowledge of the $B^{\text{tip}}_{||}(x, y)$ distribution in a 2D plane suffices to calculate all vector components of $\vec{B}^{\text{tip}}(x, y)$ (see Supplemental Material [29]). Fig. 2(d) shows the calculated out-of-plane component B^{tip}_z of the tip stray field which is used to calibrate the MFM measurements [31]. B^{tip}_z has a maximum with the tip situated above the NV center and shows the expected rotational symmetry.
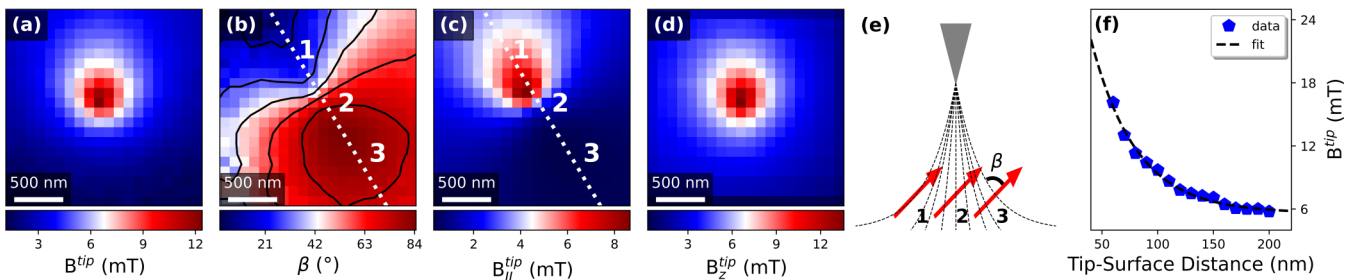
FIG. 2. Characterization of MFM tip stray field by NV magnetometry. The tip is scanned at $z = 80$ nm above the diamond surface. (a) Two-dimensional (2D) map of magnitude of the tip field B^{tip}. (b) 2D map of field angle β relative to the NV axis. The symmetry axis (dashed line) corresponds to the in-plane orientation of the NV axis. (c) map of $B^{\text{tip}}_{||}$. (d) 2D map of the derived z component B^{tip}_z of the tip stray field. The 2D distribution of $B^{\text{tip}}_z(x, y)$ is the key ingredient for quantum calibration of the MFM. (e) Sketch of the relative angle β of the tip stray field and the NV axis. (f) Tip-surface distance dependence of B^{tip} with the tip positioned above the NV center. From interpolation (dashed line) a maximum tip stray field of 44 mT at the tip apex is derived.
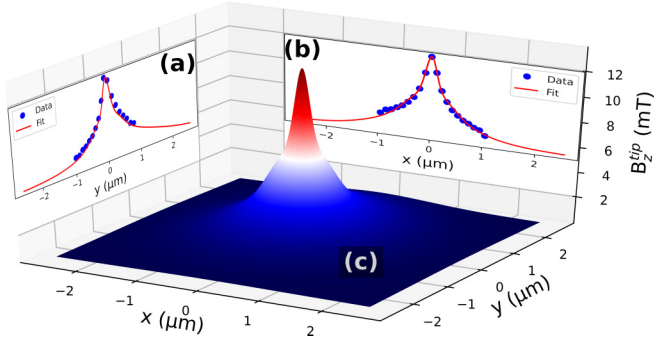
FIG. 3. Quantum calibrated tip stray-field distribution. (a), (b) Sections in x- and y direction through the maximum of the B_z^{tip} data of Fig. 2(e) (blue solid symbols). The red lines show combined Gaussian-Voigt fits to the data. (c) Quantum calibrated tip stray-field distribution $B_z^{\mathrm{tip,NV}}(x, y)$ based on the extrapolated data fits of (a), (b). The fits are used to extrapolate the NV measured stray field to an area of 5.11 μm $\times$ 5.11 μm to consider longer-range magnetic interactions between tip and sample.

Additionally, B^{tip} was measured as function of the tip-surface distance with the tip positioned near the maximum of B^{tip} [Fig. 2(f)]. The data were measured without cantilever oscillation with the zero tip-sample distance defined by a repulsive tip-sample force of 2.66 nN. The measured field decrease with increasing distance is well described by an exponential decay (dashed line). By extrapolating to zero distance, we derive a maximum tip stray field of around 44 mT at the tip apex. This compares well with stray-field estimations from qMFM calibration procedures for similar low-moment tips [15].

In qMFM, the measured MFM signal is related to the quantitative stray-field distribution by the so-called instrument calibration function, ICF, being the calibrated point-spread function of the imaging process. A major contribution to the ICF is the tip stray-field distribution $B_z^{\mathrm{tip}}(x, y)$, which determines the spatial broadening associated with the MFM measurement. In 2D Fourier space the formula governing these relations reads as follows [7] (see Supplemental Material [29]):

$$\Delta\Phi(k, z) = ICF(\boldsymbol{k}) \cdot B_z^{\mathrm{sample}}, \text{ with}$$

$$ICF(\boldsymbol{k}) = \frac{2\,Q}{C\,\mu_0}\ [LCF\,(k, \Theta, A)]^2 k e^{kz} B_z^{\mathrm{tip*}}(k, 0) \quad (1)$$

Q and C are the quality factor and the stiffness of the oscillating cantilever, the LCF corrects for the finite oscillation amplitude A and canting angle Θ of the cantilever.

The NV data of Fig. 2(d) directly deliver a quantum calibrated $B_z^{\mathrm{tip,NV}}(x, y)$. Figures 3(a) and 3(b) show linear sections of $B_z^{\mathrm{tip,NV}}(x, y)$ along x and y through the maximum of Fig. 2(d). The blue measured data points are shown together with fits (red lines) to the data. The fits are used to extrapolate the measured stray-field data to field values outside the 2-μm $\times$ 2-μm measurement window to consider longer-range magnetic interactions. The according 2D extrapolated stray-field distribution [Fig. 3(c)] shows a sharp maximum of around 14 mT and a slight distortion of the rotational symmetry mostly resulting from the tilt of the MFM cantilever [Figs. 1(a) and 1(d)]. This NV measured stray-field distribu-

tion of the tip $B_z^{\mathrm{tip,NV}}(x, y)$ in combination with the cantilever's mechanical properties yield the quantum calibrated ICF. Using this quantum calibrated ICF, any consecutive MFM measurements can be directly converted into quantum calibrated QuMFM stray-field maps without requiring knowledge on the sample.

The principle of MFM measurements is schematically sketched in Fig. 1(d). As a test sample we use a Co/Pt multilayer with perpendicular magnetic anisotropy (PMA) that shows perpendicular stripe domains with 170-nm average domain width (for details, see Supplemental Material [29]). It exhibits a maximum stray field of about 100 mT at a few tens of nm surface distance, a field range typical for many industrially relevant thin films but inaccessible for direct quantitative mapping by scanning NV magnetometry. Furthermore, the sample is a typical reference material for classical qMFM calibration [32]. This sample was chosen since, for this particular PMA material, the sample stray fields can also independently be estimated, based on the well-characterized global sample properties, from the MFM phase-shift measurement (see Supplemental Material Sec. G and below) and thus it allows to compare its QuMFM stray-field maps to an independent source of knowledge. For MFM measurements, the surface topography is first determined by a scan in intermittent contact mode. Then, in a second scan at height z_{tot}, the phase shift $\Delta\Phi$ of the cantilever oscillation is sampled. It is caused by the magnetic tip-sample interactions and constitutes the MFM raw data of Fig. 4(a). MFM data were collected in a scan range of $(5.11\,\mu\mathrm{m})^2$ with 512×512 pixels. The cantilever spring constant $C = (3.159 \pm 0.442)\,\mathrm{N/m}$ was determined from thermal fluctuations and the resonance quality factor $Q = 160.7 \pm 5$ from the resonant oscillation peak at z_{tot}. Two consecutive cycles of NV calibrations and MFM measurements delivered comparable results, speaking for a good stability of the MFM tip under the given calibration and measurement conditions.

Exploiting the relation from Eq. (1), the QuMFM measured quantum calibrated stray-field distribution B_z^{QuMFM} at height $z_{\mathrm{tot}} = 80$ nm [Fig. 4(b)] is then derived by a deconvolution of the raw data of Fig. 4(a) with the quantum calibrated ICF using a pseudo-Wiener filter for regularization. The regularization parameter is chosen such that the instrument noise is filtered without significantly cutting contributions from the stray-field spectrum. We would like to note again that the calculation of the quantitative stray-field distribution B_z^{QuMFM} from the measured phase-shift data $\Delta\Phi$ merely requires the NV calibrated tip stray-field data $B_z^{\mathrm{tip,NV}}$, and that no prior knowledge on the sample magnetic properties is needed. Such a calculation is possible for any sample, independent of its magnetization distribution.

Figure 4(g) compares sections of the reconvolved Wiener-filtered MFM data (red) with the initial experimental MFM data (green) as a check of consistency. They agree well, speaking for a moderate accuracy loss due to filtering. More details on the data analysis and deconvolution procedures are given in the Supplemental Material, Sec. D.

Figure 4(c) shows the estimated reference stray field B_z^{ref} at $z_{\mathrm{tot}} = 80$. For the calculation, the MFM raw data are first deconvolved with $B_z^{\mathrm{tip,NV}}(x, y)$ to reduce the feature

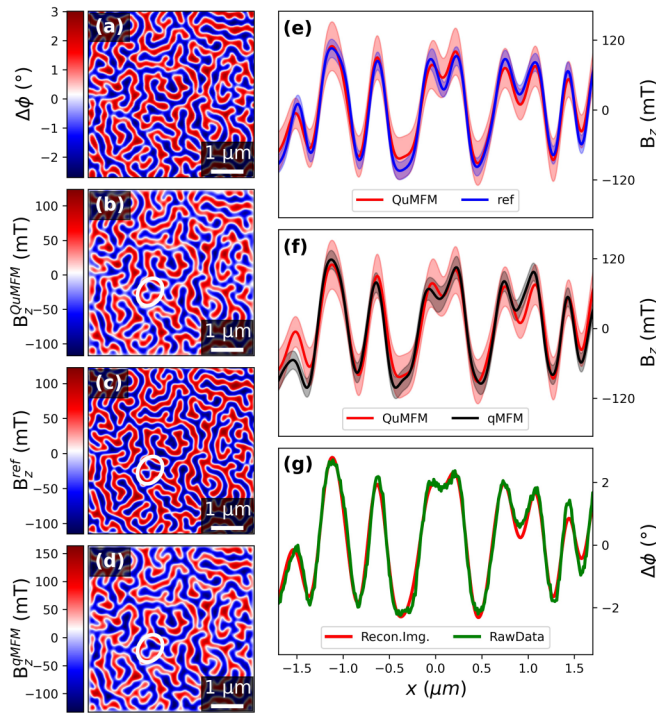FIG. 4. Quantum calibrated MFM. (a) MFM data of the Co/Pt multilayer sample with characteristic stripe domains. (b) Quantum calibrated B_z^{QuMFM} at a tip surface distance of 80 nm, obtained from a deconvolution of the MFM data with the instrument calibration function based on the quantum calibrated $B_z^{\mathrm{tip,NV}}$ of Fig. 3(c). (c) Calculated B_z^{ref} based on the discriminated domain pattern after deconvolution with $B_z^{\mathrm{tip,NV}}(x, y)$. (d) Classical qMFM image of the sample's stray field obtained from a deconvolution of the MFM data with a conventionally estimated instrument calibration function. The white ellipses in (b)–(d) mark characteristic differences of quantum calibrated QuMFM and classical qMFM (see text). (e), (f) Comparison of horizontal cross sections of B_z of (b)–(d) in the center of the images. Uncertainty bands are plotted as shaded regions. (e) Comparison of B_z^{QuMFM} (b, red) and B_z^{ref} (c, blue). The data agree well within the uncertainty. (f) Comparison of B_z^{QuMFM} (b, red) and B_z^{qMFM} (d, black). The data again agree within the uncertainty bands. (g) Test of regularized deconvolution procedure applied in (b). The raw MFM data and the reconvolved data show very good agreement.

broadening induced by the imaging process and then discriminated, resulting in a well-founded guess of the domain pattern. In a second step, from the associated surface charge pattern (both at the upper and lower surface of the film) and the transition at the domain boundaries, the stray field B_z^{ref} is calculated at the desired height above the sample surface. Details are described in the Supplemental Material, Sec. E.

Figure 4(d) shows the B_z^{qMFM} data as obtained by conventional qMFM [32]. In a conventional calibration $B_z^{\mathrm{tip}}(x, y)$ is not known *a priori*. Hence, the guess of the reference domain pattern is derived by directly discriminating the raw data of Fig. 4(a) [i.e., without prior deconvolution with $B_z^{\mathrm{tip}}(x, y)$]. This simplified guess of the stray-field distribution is used to derive the classical *ICF* and hence to calibrate the data.

Figure 4(e) compares horizontal sections through Figs. 4(b) and 4(c) at the center of the images. B_z^{QuMFM}

is shown in red and B_z^{ref} in blue. The data agree well within the uncertainty bands (shaded regions), thereby affirming the credibility of the quantum calibration. For the given calibration we derive an uncertainty of B_z^{QuMFM} of $u_{\mathrm{tot}} = 20\%$ for fields around 100 mT (see Supplemental Material [29]). u_{tot} is dominated by the rather large uncertainty of the cantilever's spring constant C ($u_C = 14\%$) and the resonance quality factor Q ($u_Q = 3\%$). Smaller contributions stem from the uncertainty of the tip-sample distance during tip calibration and MFM measurement, as well as from MFM noise and numerical uncertainties (see Supplemental Material [29]). With respect to u_{tot} the field uncertainty of the ODMR data can be neglected. The main uncertainty contribution of the model fields B_z^{ref} of 6% stems from the sample's saturation magnetic moment m_s. Figure 4(f) compares B_z^{QuMFM} (red) and B_z^{qMFM} (black). The agreement of the data within the uncertainty bands can be considered independent validation of the classical qMFM calibration. However, since the *ICF* of qMFM is derived from the MFM image without prior knowledge of the broadening of magnetic features by the tip [31], the *ICF*'s sharpness is overestimated and hence narrow stray-field features are suppressed. An example illustrating this effect is marked by the ellipses in Figs. 4(b)–4(d), where a narrow domain feature found in B_z^{QuMFM} and B_z^{ref} is not revealed in B_z^{qMFM}.

Quantum calibrated QuMFM as demonstrated here has several advantages over qMFM. Besides being quantum traceable, it does not rely on a reference sample and its properties. In qMFM, the *ICF* calibration is only reliable in the range of spatial wave vectors k of the reference sample's magnetic features. Larger and smaller structures cannot be quantitatively measured. In QuMFM, the NV measurement of the tip's stray field can be performed over high-density spatial grids for sampling large-k data, but also over large areas below the tip apex for quantifying the low-k contributions of $B_z^{\mathrm{tip,NV}}$. Thus, QuMFM with a such calibrated tip can be applied to magnetic stray-field landscapes containing any length scales, also combining nanometer and micrometer feature sizes. The smoothness of the tip's B_z^{tip} profile even allows using an adapted, nonuniform mesh in the NV measurements, which renders such multiscale calibration feasible. This will in the future enable quantitative studies of magnetic multiscale phenomena, e.g., interaction domains in nanocrystalline permanent magnet samples [33], which cannot be analyzed quantitatively so far. Additionally, the quantitative knowledge of the tip stray field allows evaluating its backaction on the domain structure of the magnetic sample and will enable quantitative investigations of tip field-induced manipulation of nanomagnetic objects [15,34]. Furthermore, this knowledge makes it possible to select a suitable type of tip which will interact with the sample in a negligible way concerning its impact on the sample's magnetization.

Note that in the future significantly improved QuMFM field uncertainties can be foreseen. Especially, the dominating uncertainty of the cantilever spring calibration could be drastically reduced to <1% by proper calibration [35,36]. Vacuum MFM with orders of magnitude higher Q factor and thus better signal to noise should allow a further reduction of the total uncertainty down to about 1% or less.

Obviously, the tip calibration procedure demonstrated above is too time-consuming to be performed routinely for everyday MFM use. Here, the most promising route to quantum traceable MFM measurements is to provide quantum traceably calibrated transfer standards. Note that the data of Fig. 4(b) also represent quantum traceable calibration of the stray field of a Co/Pt qMFM reference sample which, with a domain transition width of 15–20 nm and a typical domain size of about 200 nm, has been successfully used in various studies [9,15,37] for conventional qMFM on magnetic feature sizes from 30 nm to about 1 μm. In the future, qMFM can be based on the *NV measured* QuMFM stray-field distribution B_z^{QuMFM} circumventing the systematic errors of B_z^{ref} discussed above. This will turn reference sample-based qMFM calibrations into quantum traceably calibrated stray-field measurements. Additionally, the QuMFM calibration will allow developing reference samples with different magnetic properties tailored to specific applications and field ranges since the reference sample's properties are no longer dictated by the hard requirement of a calculable domain model. This opens the way for widely available quantum traceable nanoscale magnetic measurements over a broad field range using virtually any MFM.

[1] N. Romming, A. Kubetzka, C. Hanneken, K. von Bergmann, and R. Wiesendanger, Field-Dependent Size and Shape of Single Magnetic Skyrmions, Phys. Rev. Lett. **114**, 177203 (2015).

[2] Y. Dovzhenko, F. Casola, S. Schlotter, T. X. Zhou, F. Büttner, R. L. Walsworth, G. S. D. Beach, and A. Yacoby, Magnetostatic twists in room-temperatureskyrmions explored by nitrogen-vacancy center spin texture reconstruction, Nat. Commun. **9**, 2712 (2018).

[3] M. Baćani, M. A. Marioni, J. Schwenk, and H. J. Hug, How to measure the local Dzyaloshinskii-Moriya interaction in skyrmion thin-film multilayers, Sci. Rep. **9**, 3114 (2019).

[4] X. Zhao, J. Schwenk, A. O. Mandru, M. Penedo, M. Baćani, M. A. Marioni, and H. J. Hug, Magnetic force microscopy with frequency-modulated capacitive tip-sample distance control, New J. Phys. **20**, 13018 (2018).

[5] K. Y. Meng, A. S. Ahmed, M. Baćani, A. O. Mandru, X. Zhao, N. Bagués, B. D. Esser, J. Flores, D. W. McComb, H. J. Hug, and F. Yang, Observation of nanoscale skyrmions in SrIrO$_3$/SrRuO$_3$ bilayers, Nano Lett. **19**, 3169 (2019).

[6] O. Kazakova, R. Puttock, C. Barton, H. Corte-León, M. Jaafar, V. Neu, and A. Asenjo, Frontiers of magnetic force microscopy, J. Appl. Phys. **125**, 60901 (2019).

[7] H. J. Hug, B. Stiefel, P. J. A. Van Schendel, A. Moser, R. Hofer, S. Martin, H. J. Güntherodt, S. Porthun, L. Abelmann, J. C. Lodder, G. Bochi, and R. C. O'Handley, Quantitative magnetic force microscopy on perpendicularly magnetized samples, J. Appl. Phys. **83**, 5609 (1998).

[8] T. Kebe and A. Carl, Calibration of magnetic force microscopy tips by using nanoscale current-carrying parallel wires, J. Appl. Phys. **95**, 775 (2004).

[9] S. Vock, C. Hengst, M. Wolf, K. Tschulik, M. Uhlemann, Z. Sasvári, D. Makarov, O. G. Schmidt, L. Schultz, and V. Neu, Magnetic vortex observation in FeCo nanowires by quantitative magnetic force microscopy, Appl. Phys. Lett. **105**, 172409 (2014).

[10] H. Corte-León, V. Neu, A. Manzin, C. Barton, Y. Tang, M. Gerken, P. Klapetek, H. W. Schumacher, and O. Kazakova, Comparison and validation of different magnetic force microscopy calibration schemes, Small **16**, 1906144 (2020).

[11] S. McVitie, R. P. Ferrier, J. Scott, G. S. White, and A. Gallagher, Quantitative field measurements from magnetic force microscope tips and comparison with point and extended charge models, J. Appl. Phys. **89**, 3656 (2001).

[12] D. V. Ovchinnikov and A. A. Bukharaev, Computer simulation of magnetic force microscopy images with a static model of magnetization distribution and dipole-dipole interaction, Tech. Phys. **46**, 1014 (2001).

[13] N. S. Kiselev, I. E. Dragunov, V. Neu, U. K. Rößler, and A. N. Bogdanov, Theoretical analysis of magnetic force microscopy contrast in multidomain states of magnetic superlattices with perpendicular anisotropy, J. Appl. Phys. **103**, 043907 (2008).

[14] V. Neu, S. Vock, T. Sturm, and L. Schultz, Epitaxial hard magnetic SmCo$_5$ MFM tips-a new approach to advanced magnetic force microscopy imaging, Nanoscale **10**, 16881 (2018).

[15] S. Zhang, J. Zhang, Q. Zhang, C. Barton, V. Neu, Y. Zhao, Z. Hou, Y. Wen, C. Gong, O. Kazakova, W. Wang, Y. Peng, D. A. Garanin, E. M. Chudnovsky, and X. Zhang, Direct writing of room temperature and zero field skyrmion lattices by a scanning local magnetic field, Appl. Phys. Lett. **112**, 132405 (2018).

[16] C. Di Giorgio, A. Scarfato, M. Longobardi, F. Bobba, M. Iavarone, V. Novosad, G. Karapetrov, and A. M. Cucolo, Quantitative magnetic force microscopy using calibration on superconducting flux quanta, Nanotechnology **30**, 314004 (2019).

[17] L. Kong and S. Chou, Quantification of magnetic force microscopy using a micronscale current ring, Appl. Phys. Lett. **70**, 2043 (1997).

[18] P. Rice, S. Russek, and B. Haines, Magnetic imaging reference sample, IEEE Trans. Magn. **32**, 4133 (1996).

[19] P. Rice, S. Russek, J. Hoinville, and M. Kelley, in *Proceedings of the Fourth Workshop on Industrial Applications of Scanned Probe Microscopy*, The NIST Magnetic Imaging Reference Sample, Gaithersburg, MD, USA (NIST, Gaithersburg, Maryland, US, 1997).

[20] S. Signoretti, C. Beeli, and S. H. Liou, Electron holography quantitative measurements on magnetic force microscopy probes, J. Magn. Magn. Mater. **272–276**, 2167 (2004).

[21] V. N. Matveev, V. I. Levashov, V. T. Volkov, O. V. Kononenko, A. V. Chernyh, M. A. Knjazev, and V. A. Tulin, Fabrication and use of a nanoscale Hall probe for measurements of the magnetic field induced by MFM tips, Nanotechnology **19**, 475502 (2008).

[22] V. Panchal, Ó. Iglesias-Freire, A. Lartsev, R. Yakimova, A. Asenjo, and O. Kazakova, Magnetic scanning probe calibration using graphene Hall sensor, IEEE Trans. Magn. **49**, 3520 (2013).

[23] J. Scott, S. McVitie, R. P. Ferrier, G. P. Heydon, W. M. Rainforth, M. R. J. Gibbs, J. W. Tucker, H. A. Davies, and J. E. L. Bishop, Characterisation of FeBSiC coated MFM tips using Lorentz electron tomography and MFM, IEEE Trans. Mag. **35**, 3986 (1999).

[24] J. Scott, S. McVitie, R. P. Ferrier, and A. Gallagher, Electrostatic charging artefacts in Lorentz electron tomography of MFM tip stray fields, J. Phys. D: Appl. Phys., **34**, 1326 (2001).

[25] G. Balasubramanian, I. Y. Chan, R. Kolesov, M. Al-Hmoud, J. Tisler, C. Shin, C. Kim, A. Wojcik, P. R. Hemmer, A. Krueger, T. Hanke, A. Leitenstorfer, R. Bratschitsch, F. Jelezko, and J. Wrachtrup, Nanoscale imaging magnetometry with diamond spins under ambient conditions, Nature (London) **455**, 648 (2008).

[26] M. W. Doherty, N. B. Manson, P. Delaney, F. Jelezko, J. Wrachtrup, and L. C. L. Hollenberg, The nitrogen-vacancy colour centre in diamond, Phys. Rep. **528**, 1 (2013).

[27] C. L. Degen, F. Reinhard, and P. Cappellaro, Quantum sensing, Rev. Mod. Phys. **89**, 035002 (2017).

[28] C. Müller, X. Kong, J. M. Cai, K. Melentijević, A. Stacey, M. Markham, D. Twitchen, J. Isoya, S. Pezzagna, J. Meijer, J.

F. Du, M. B. Plenio, B. Naydenov, L. P. McGuinness, and F. Jelezko, Nuclear magnetic resonance spectroscopy with single spin sensitivity, Nat. Commun. **5**, 4703 (2014).

[29] See Supplemental Material at http://link.aps.org/supplemental/10.1103/PhysRevB.104.214427 for the detailed measurements and calculations of the NV experiments, deconvolution algorithm used for MFM measurements, magnetic field calculations and conversion of the field components, reference and test sample stray-field calculations, mechanical properties of the cantilever, uncertainty estimations, and repetitive measurement consistencies.

[30] A. Gruber, A. Dräbenstedt, C. Tietz, L. Fleury, J. Wrachtrup, and C. Von Borczyskowski, Scanning confocal optical microscopy and magnetic resonance on single defect centers, Science **276**, 2012 (1997).

[31] F. Casola, T. van der Sar, and A. Yacoby, Probing condensed matter physics with magnetometry based on nitrogen-vacancy centres in diamond, Nat. Rev. Mater. **3**, 17088 (2018).

[32] X. Hu, G. Dai, S. Sievers, A. Fernández-Scarioni, H. Corte-León, R. Puttock, C. Barton, O. Kazakova, M. Ulvr, P. Klapetek, M. Havlíček, D. Nečas, Y. Tang, V. Neu, and H. W. Schumacher, Round robin comparison on quantitative nanometer scale magnetic field measurements by magnetic force microscopy, J. Magn. Magn. Mater. **511**, 166947 (2020).

[33] J. Thielsch, H. Stopfel, U. Wolff, V. Neu, T. G. Woodcock, K. Güth, L. Schultz, and O. Gutfleisch, In situ magnetic force microscope studies of magnetization reversal of interaction domains in hot deformed Nd-Fe-B magnets, J. Appl. Phys. **111**, 103901 (2012).

[34] A. Casiraghi. H. Corte-León, M. Vafaee, F. Garcia-Sanchez, G. Durin, M. Pasquale, G. Jakob, M. Kläui, and O. Kazakova, Individual skyrmion manipulation by local magnetic field gradients, Commun. Phys. **2**, 145 (2019).

[35] M. S. Kim, J. R. Pratt, U. Brand, and C. W. Jones, Report on the first international comparison of small force facilities: A pilot study at the micronewton level, Metrologia **49**, 70 (2012).

[36] V. Nesterov, O. Belai, D. Nies, S. Buetefisch, M. Mueller, T. Ahbe, D. Naparty, R. Popadic, and H. Wolff, SI-traceable determination of the spring constant of a soft cantilever using the nanonewton force facility based on electrostatic methods, Metrologia **53**, 1031 (2016).

[37] R. Puttock, A. Manzin, V. Neu, F. Garcia-Sanchez, A. Fernandez Scarioni, H. W. Schumacher, and O. Kazakova, Modal frustration and periodicity breaking in artificial spin ice, Small **16**, 2003141 (2020).